ONSET OF OIL MOBILIZATION AND NON-WETTING PHASE CLUSTER SIZE DISTRIBUTION

S.Berg[1], R. T. Armstrong[1], A. Georgiadis[1], H. Ott[1], A. Schwing[1], R. Neiteler[1],
N. Brussee[1], A. Makurat[1], M. Rücker[2,1], L. Leu[1,2], M. Wolf[2], F. Khan[2], F. Enzmann[2], M. Kersten[2]

[1]Shell Global Solutions International BV, The Netherlands.
[2]Geosciences Institute, Johannes-Gutenberg University, 55099 Mainz, Germany

This paper was prepared for presentation at the International Symposium of the Society of Core Analysts held in Avignon, France, 8-11 September, 2014

ABSTRACT

The onset of oil mobilization during imbibition has been imaged with pore scale resolution under dynamic flow conditions visco-capillary balance, by using fast synchrotron-based X-ray computed micro tomography. Oil mobilization under unsteady-state displacement has been studied for sintered glass, sandstone and carbonate rock, which demonstrate distinctly different behavior with respect to the cluster-size distributions and respective time evolution.

For the sandstone sample, which showed the largest saturation change between the three samples, over 50% of the oil was mobilized during imbibition. The cluster-size distribution computed from the tomography images, but also detailed visualization at the pore scale revealed that during imbibition the largest (initially connected) cluster breaks off into smaller segments. Over time successively larger segments break off which increases the frequency of intermediate size clusters. In most cases, each segment breaks off into even smaller segments, but also in fewer cases clusters merge and increase in size.

These findings support the view that at the onset of oil mobilization clusters rather break off instead of moving as a large cluster, which gives further insight into the ganglion dynamics flow regime. It is also shown that imbibition dynamics is more complex than assumed under common percolation models, where for instance disconnected non-wetting phase clusters become immobile and remain static. The experimental data instead clearly show time evolution for disconnected clusters that can lead to re-connection or further break off.

INTRODUCTION

During the production of an oil reservoir by water flooding (in a water-wet e.g. sandstone rock) the non-wetting phase (oil) is displaced by the wetting phase (water). During this

imbibition process, more than 50% of the initial oil can be trapped in the pore space, which is referred to as remaining or residual oil. This trapping is mainly attributed to capillary-dominated processes which until very recently [7] have been directly observed only in model systems like 2D micro-models [12]. As a consequence, very little is known about how trapping actually occurs in 3D real rock and what the transient process is from an overall connected oil phase to disconnected and trapped oil clusters. Most of the current macroscopic descriptions are either phenomenological, based on invasion percolation models [6, 21, 22] or pore network modeling [16], which (with few exceptions [9, 11]) consider only local elementary pore scale processes [12] like snap-off [17] but do not honor the complexity of pore scale displacement physics like ganglion dynamics [3] and cooperative processes [2] that involve both capillary and viscous forces at the same time [14].

The main reason for the lack of insight has been the inability to directly image such processes in real rock and under dynamic flow conditions. While the imaging of trapped (static) clusters at the end of imbibition has been feasible for more than a decade [10, 20], not until recently has micro X-ray computed tomography advanced enough to allow for the imaging of pore scale displacement processes like Haines jumps [8] and snap-off [17] in real-time and under dynamic flow conditions [4]. In the present study, we used this technique to study imbibition. We focus on two particular aspects: the time-evolution of the non-wetting phase cluster size distribution and the detailed pore scale processes leading to break off of oil clusters. Finally, we compare our results with a few predictions provided by percolation theory.

METHODS AND MATERIALS

As porous media, we used: sintered glass (Robuglas), Gildehauser sandstone (Bentheimer type) and Estaillades limestone. Dry μ-CT scans are displayed in Figure 1. The 3D-images were obtained by fast synchrotron-based X-ray computed micro tomography at the TOMCAT beamline (Paul Scherer Institute, Swiss Light Source) at a resolution of 2.2 μm. Cylindrical samples (4 mm diameter and 10 mm length) were embedded into polycarbonate by heat-shrinking and mounted on a sample holder for the flow experiments. The sample holder provides an integrated micro-piston-pump for fluid injection. More details about the method are described in [5]. N-decane was used as non-wetting phase and brine as the wetting phase. The interfacial tension between both fluids is 35 mN/m [5].

The sintered glass has a porosity of 35% and permeability of 22±2 D. The injection rate was 10^8 μm^3/min and the resulting microscopic capillary number $Ca_{micro} = \mu_w v / \sigma$ for this experiment is 3.9×10^{-5} [1]. The saturation remained constant during the low-rate imbibition. The reason for this behavior could be the absence of corner flow in sintered glass as all structures are very round (as a result of the sintering). Corner flow [14] has a major impact during imbibition e.g. for snap-off causing the breakup of connected oil phases.
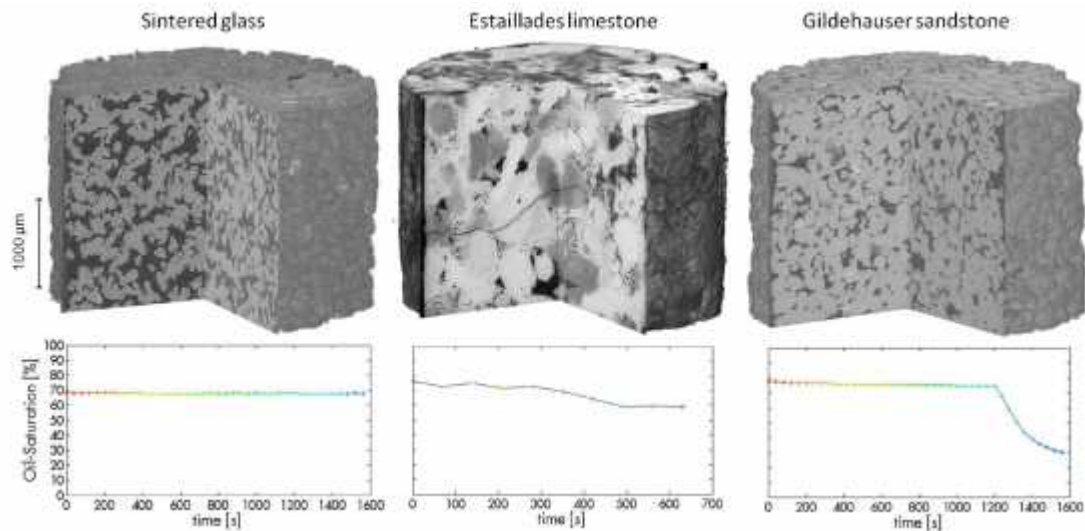
Figure 1: The different porous media imaged with synchrotron based x-ray computed micro tomography during imbibition. Top: μCT scans. Bottom: respective oil saturation as a function of time during the imbibition experiment. The color coding is used in the later figures to parameterize time.

The Estaillades limestone has a complex pore morphology. It is essentially a dual-porosity system with macro pores that are well-resolved by μCT but also micro-pores smaller than the resolution, and cracks larger than the field of view. Because its low porosity (11%) and permeability (200±6 mD) we chose for the Estaillades experiment an injection rate of 10^9 μm^3/min for the first scans and 5×10^9 μm^3/min for the last few scans resulting in $Ca_{micro} = 1.2 \times 10^{-3}$. Only very little oil mobilization was observed which could be caused by the dual-porosity structure, and due to limitations in resolutions we cannot track what happens in the micro pores. The Gildehauser sandstone, with porosity = 20%, permeability = 1.5±0.3 D, an injection rate = 10^8 μm^3/min and $Ca_{micro} = 6.8 \times 10^{-5}$, showed the most interesting behavior: during the experiment 60% of the oil (in total 2.5×10^9 μm^3) was mobilized. Therefore here we mainly present results for the Gilderhauser sample.

Image processing was performed with Avizo (Visualization Science Group), as previously described in [5] and [7]. First the data were filtered with a non-local mean filter. In the second step the flow experiment scans were registered to a scan of the dry sample. This step is necessary to get the same orientation in the dry scan and the images at each measured time step. Then the high resolution dry scan can be used to mask the pore space of the sample. Using this approach it is easier to determine fine pore structures like pore throats, which are crucial to determine the connectivity of oil and hence cluster sizes properly and are not easily resolved in the fast-scan data. The image segmentation was carried out with a watershed based segmentation routine. These segmented data were used for visualization and further analysis. The cluster size distribution was calculated using logarithmic binning with MatLab (MathWorks Inc) and the pore size distribution was calculated with GeoDict (Math2Market) using a morphological approach [19, 18].

To characterize the flow regime (capillary vs. viscous dominated flow) we used a macroscopic or cluster-based definition of the capillary number [13]

$$Ca^{macro} = \frac{l^{cl}}{r^p}\phi\frac{\mu_w v}{\sigma}$$

with the averaged cluster length (l^{cl}), radius of a pore throat (r_p), porosity (ϕ), viscosity of the non-wetting phase (μ_w), velocity (v) and interfacial tension (σ). The averaging procedure for l^{cl} is described in [1]. For the pore throat radius we used the peak of the pore size distribution calculated by GeoDict. The calculated Ca^{macro} for Gildehauser sandstone was between 1.6×10^{-3} and 2.3×10^{-3} (Capillary number for sintered glass: 1.3×10^{-3} and for Estaillades limestone: between 1.476×10^{-1} and 3.41×10^{-2}).

RESULTS

Mobilization of oil during imbibition

The oil saturation of Gildehauser sandstone initially decrease very little before rapidly decreased from 75% to 30% oil saturation at about 1200 s, as displayed in Figure 2 (left).
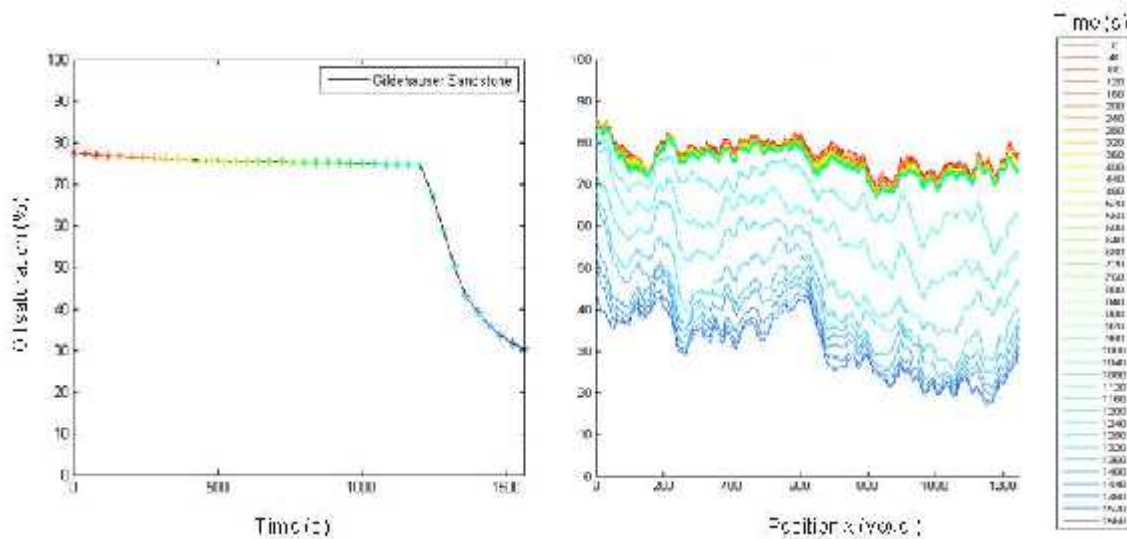

Figure 2: The oil saturation shows after 1200 s a sharp decrease indicating the mobilization of oil by the imbibition process (left). The respective saturation profiles (oil saturation as a function of position for the same times, right) shows accordingly a decrease with practically homogeneous saturation profiles slightly shifted to lower saturations close to the outlet.

The calculated Ca^{macro} for Gildehauser sandstone was between 1.6×10^{-3} and 2.3×10^{-3}, which indicates that the viscous forces were not sufficient to mobilize clusters [1] and the observed mobilization is capillary dominated, which is why we observe a large residual oil saturation at the end of imbibition.

The oil mobilization occurred simultaneously over the entire sample, as shown in the saturation profiles along the sample that are displayed in Figure 2 (right). However, the inlet side of the sample lost more oil than the outlet side, which might be indicative of a small capillary end-effect [23], so expected for low capillary number.

Cluster size distribution

In Figure 3 the resulting cluster size distributions for the Gildehauser sandstone are displayed. Clusters range from 100 µm^3 to 4.07x10^9 µm^3.
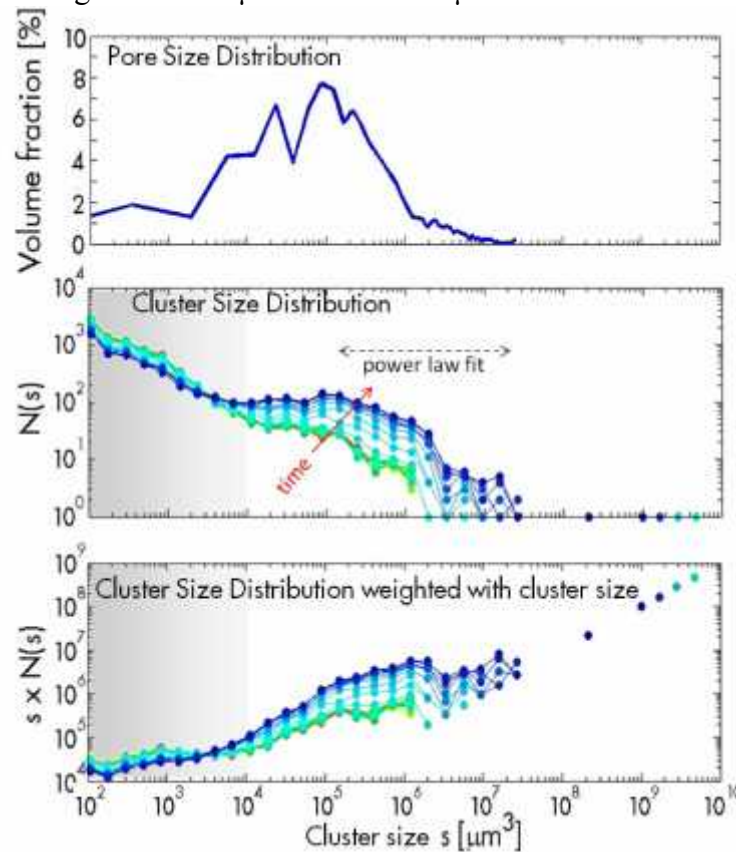

Figure 3: Pore size distribution (top), cluster size distribution (middle) and cluster size distribution
weighted with cluster size to indicate contribution to overall saturation (bottom) for Gildehauser
sandstone as a function of time during imbibition (time color coding from Figure 2).

The distribution and configuration of the oil in the pore space and its evolution during imbibition can be further characterized via the oil cluster size distribution [22, 10, 7]. The cluster sizes obtained by voxel counting of the segmented image were binned logarithmically to have an approximately similar counting statistics in each bin over the whole range [15]. Note that for power-law like distributed data, linear binning is either appropriate for small or for large cluster sizes but not for both at the same time. The (linear) binning typically chosen leads to a "tail" for large clusters with either 1 or 0 clusters per bin which is purely a binning artifact. Logarithmic binning where the width

of bins is increasing exponentially largely reduces this artifact. Following [15] we define a bin k ranging from x_k to x_{k+1} with $x_k = x_{min}a^k$ and $x_{k+1} = x_{min}a^{k+1}$, where x_{min} is the size of one voxel, which corresponds to the smallest measurable cluster. Here we use $a = (x_{max}/x_{min})^{1/n}$ where x_{max} is the size of the largest measured cluster and n is the number of bins. For further analysis on Gildehauser sandstone we chose n = 40, since higher values become noisy. Note that when measuring power law exponents from a logarithmically binned distribution, the resulting exponent is the true exponente (α) minus 1. [15].

When considering the cluster size distribution for further analysis it is important to put the cluster sizes into perspective with the size of individual pores and indicate a range from which a cluster extends over one or more pores, i.e. identify oil blobs that are actually clusters. In Figure 3, in addition to the cluster size distributions also the pore size distribution is plotted in the top panel. Up to cluster sizes $s \sim 10^5$ μm^3, clusters extend only over a fraction of a pore. That is also displayed in the example shown in Figure 4 where a representative cluster for each size order of magnitude is displayed. For a comparison with e.g. percolation theory, only clusters of one pore and larger are considered [22].
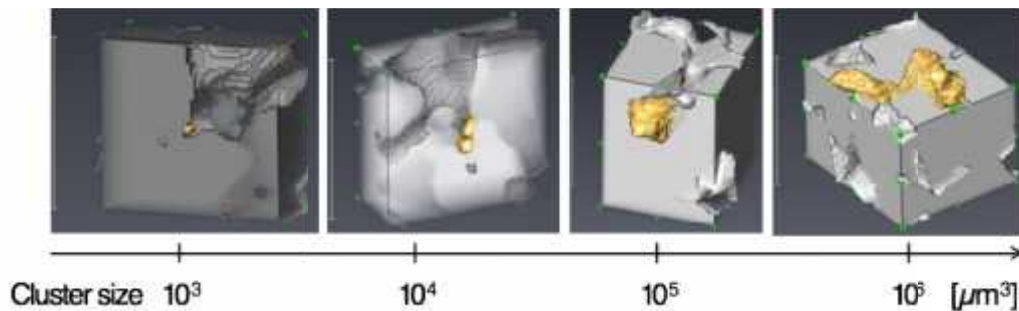
Figure 4: Clusters of different sizes in the pore space. Clusters up to 10^4 μm^3 are mostly smaller than a pore, clusters between 10^4 μm^3 and 10^5 μm^3 fill a whole pore and clusters larger than 10^5 μm^3 occupy more than one pore.

One can clearly observe that during imbibition, the number of clusters equal to and larger than individual pores estimated from the pore size distribution displayed in the top panel of Figure 3 increase during imbibition. Meanwhile, the largest cluster decreases in size. The cluster size distribution weighted by cluster size (bottom panel of Figure 3) illustrates the contribution of cluster sizes to overall saturation. Initially, the largest cluster contains 99.24% of the total oil volume in the sample and at the end of the experiment only 56.31% of all oil is in the largest cluster. During imbibition, the largest cluster lost a total volume of 3.2 x10^9 μm^3 from which 2.5 x10^9 μm^3 of oil was mobilized and produced (outside the field of view) and 0.7 x10^9 μm^3 were re-distributed into medium sized clusters.

Comparison with invasion percolation

The final cluster size distribution (of trapped, immobile clusters) resulting from an imbibition process is often described by percolation models like the invasion percolation with trapping by Wilkinson and co-authors [6, 21, 22]. The basic assumption is that the invading wetting phase during imbibition randomly disconnects the non-wetting phase in pore throats of the multiply connected pore space. A non-wetting phase cluster can only be disconnected, if it has a connection to the outlet. The resulting cluster size distribution when this process is completed is described by a power-law

$$N(s) \propto s^{-\alpha}$$

where $N(s)$ is the frequency of cluster size s. For invasion percolation with trapping, $\alpha \sim 2.2$ [22] which is also compatible with some experimental findings [10, 7]. However, this exponent applies only for capillary dominated flow systems [13], depending on injection rate of the wetting phase [22], and when the imbibition process is completed.

At the end of our experiment, the imbibition process may not be fully completed and full capillary equilibrium may not yet have been reached. But we want to investigate to which extent the cluster size is already power-law like and to how close the value of α is to the value predicted by [22]. First, we have to restrict our analysis to clusters extending over one pore or larger (see Figure 4).
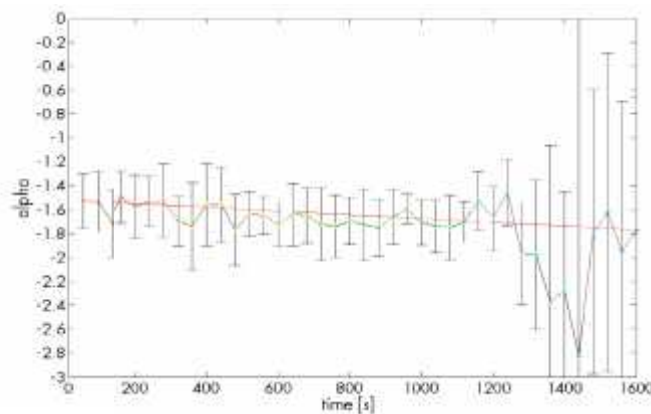

Figure 5: Development of the exponent α of the percolation theory during imbibition. Despite the relatively large error, one can observe a trend that α approaches the predicted value ($\alpha \sim 2.2$) [22] during imbibition.

We find that over a range between $10^5 < s < 10^7$ μm^3 the cluster size distribution is approximately power-law like (Figure 3, middle panel) and can be used for a power-law fit to determine α. We slightly adapted the range used for the power law fit to account for the change in cluster size distribution during the imbibition process. In Figure 5, the development of α during the imbibition process is plotted.

In our experiment, clusters are often larger than the field of view and the number of clusters larger than individual pores and not percolating to outside the field of view is limited. That leads to a non optimum counting statistics and, together with the limited range in *s* and *a* not entirely power-law like distribution, to relatively large error estimates. Nevertheless, we can see in Figure 5 that initially $\alpha < 2$ including beyond the error margins. One can also observe a trend during the imbibition to more negative values of α which starts approaching but does not fully reach the percolation value of $\alpha \sim 2.2$ [22].

Time evolution of the largest clusters during imbibition

The largest cluster contains 99.24% of the whole oil-volume at the beginning of the measurement and fills nearly the entire pore space. In the analysis below we follow the time evolution of this main percolating cluster and consider also the eight next largest clusters in order to understand how during the imbibition process oil is redistributed from the largest cluster to medium-size clusters.
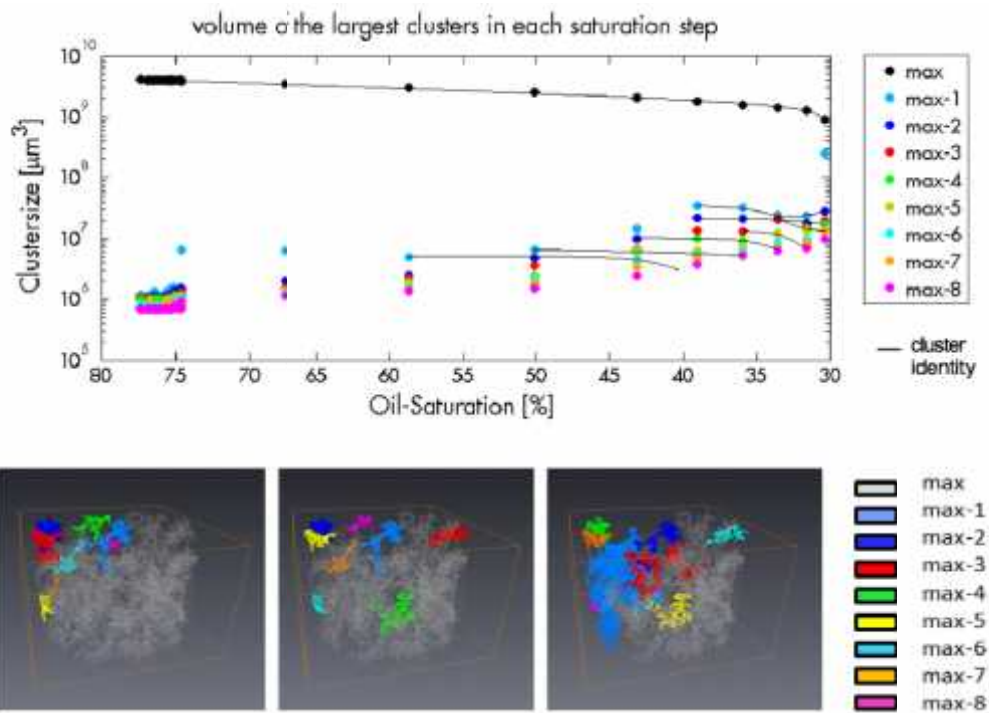

Figure 6: Development of the largest clusters during imbibition (top). While the largest cluster breaks up, the sizes of the next smaller clusters increase. According to percolation the new appearing clusters breaks up, too (cluster identity). But in rare, cases a magnification can be observed. In the bottom picture the 9 largest clusters for the last three time steps (40s) are shown.

The time evolution of the cluster size of the 9 largest clusters displayed in Figure 6 suggests that the largest cluster breaks up while the size of the next smaller clusters increases. Comparable observations were made by [7].

A closer look shows that from the largest cluster, increasingly larger segments break off. Each segment breaks up further into smaller segments. In other words, clusters are (in most cases) not growing in volume, but the new clusters which break off from the largest cluster become increasingly larger and as displayed in the top panel of Figure 6 change the order in cluster ranking (note that in Figure 6 color coding of clusters is by rank, whereas the lines represents the cluster identity). Each cluster can break further apart into smaller fragments including clusters which are not percolating to outside the field of view. Since most clusters break up at the outlet side of our sample it is not fully clear to which extent this process is influenced by a capillary end-effect.

Snap off and Coalescence

In Figure 6, in some rare cases we observed an increase in cluster size. A possible explanation of this observation is coalescence with another cluster, which we investigate in more detail. In Figure 7, we show snap-off and coalescence processes for three selected clusters.
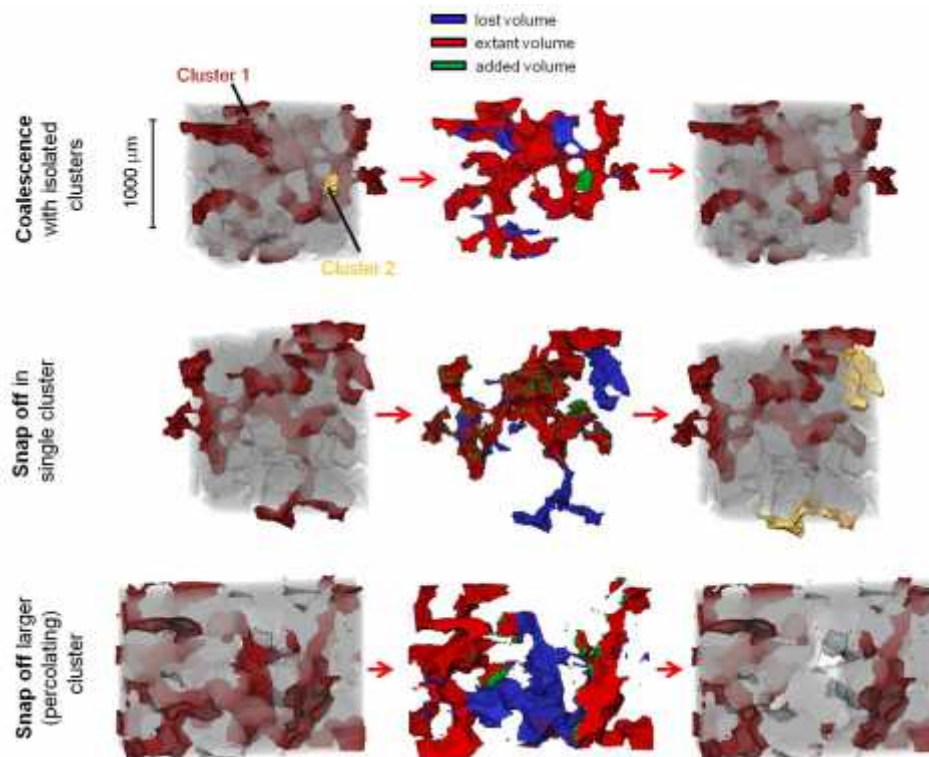
Figure 7: Snap-off and coalescence events could be observed directly and in 3D during imbibition. While coalescence (top) is rare, snap off events in different manners could be observed. Snap off occurred at narrow pore throats (middle) but also at a range of several pores (bottom).

In most cases, we observe that the break-up of clusters is caused by snap-off events. A snap-off event occurs when the capillary pressure is greater than the threshold pressure of the non-wetting phase [12]. The wetting fluid invades the pore space and forces the non-wetting fluid to disconnect [5]. Mostly, snap off occurs at narrow pore throats as shown in Figure 7 (middle) [4,14]. But, we also observed snap-off over a range of several pores (Figure 7, bottom). However, during large snap-off events an increase of the menisci in the surrounded area was measured.

In rare cases, coalescence of the non-wetting phase occurred (Figure 7, top). In combination with the observed snap off events the flow regime shows the same elements as ganglion dynamic observed in 2D-model steady state experiments [3]. However, since the capillary number (Ca^{macro}) is smaller than 1 the behavior observed here is not driven by viscous forces [13] but rather by capillary forces.

The coalescence could be caused by the fluid re-distribution after other snap off events in the vicinity, i.e. indicate also a certain level of cooperative dynamics as observed for Haines jumps in drainage [2]. While the meniscus snaps off the oil volume, which was previously stored in this region (which can exceed single pore, see Figure 7, bottom) has to redistribute. This can increase other fluid menisci and lead to coalescence with a neighboring cluster that is maybe only a pore throat apart. However, connection and disconnection of pores and clusters is difficult to determine. Pore throats are thin and the resolution of a CT-image can be too low to capture them properly. The observed clusters and pores are sometimes connected by one single voxel.

CONCLUSION

Direct real-time imaging gives important insights into the complexity of pore scale displacement processes, which occur during imbibition. In a sandstone rock sample the imbibition process was investigated at the macroscopic capillary number $Ca^{macro} < 1$ [13] indicating that the imbibition process studied here is dominated by capillary forces. Corresponding to that snap-off events are the dominant processes.

During the imbibition process largest clusters decrease in size while the medium size clusters become larger and more frequent. That points to a break up process, which was subsequently analyzed in two different ways in more detail. First, the power law exponent for the medium-size range of clusters was determined yielding exponent initially -1.6 ± 0.2 for a situation where most of the oil is contained in one large cluster. During the imbibition process where this largest cluster breaks off into smaller clusters, the exponent becomes more negative pointing into the direction of -2.0, which would be more consistent with the prediction by Wilkinson, 1986 [22] of α~2.2 for a completed invasion percolation process with trapping.

Then we focused on the 9 largest clusters only for the pore scale displacement processes and found that the break up process is dominated by snap-off processes, which results in clusters breaking off. The break up occurs mainly in thin pore throats but can also extend over multiple pores. In this way, from the largest cluster, increasingly larger segments

break off. Each segment itself breaks apart into smaller segments. In rare cases, we also observed coalescence between individual segments, attributed to potential proximate snap off events.

Those two processes clearly indicate that the imbibition dynamics is more complex than common percolation assume where disconnected non-wetting phase clusters become immobile and static [22]. The experimental data instead clearly shows time evolution for disconnected clusters that can lead for instance to re-connection or further break up.

ACKNOWLEDGMENTS

REFERENCES

*   Corresponding author; E-mail address: steffen.berg@shell.com

1. Armstrong R. T., Georgiadis, A., Ott, h., Klemin, D., Berg, S. (2014), Desaturation studied with fast X-ray computed microtomography, Geophysical Research Letters, 41, pp.55-60.
2. Armstrong, R. T. and S. Berg (2013), Interfacial velocities and capillary pressure gradients during Haines jumps, *Physical Review E*, 88(4).
3. Avraam, D. G. and Payatakes, A. C. (1995), Flow regimes and relative permeabilities during steady-state two-phase flow in porous media, *Journal of Fluid Mechanics*, 293, pp. 207-236.
4. Berg, S., Ott, H., Klapp, S. A., Schwing, A., Neiteler, R., Brussee, N., Makurat, A., Leu, L, Enzmann, F., Schwarz, J.-O., Wolf, F., Kersten, M., Irvine, S., Stampanoni, M. (2013), Real-time 3D imaging of Haines jumps in porous media flow, *Proceedings of the National Academy of Sciences*, *110*(10), 3755-3759.
5. Berg, S., Armstrong, H. Ott, S. Georgiadis, S., Klapp, S. A., Schwing, A. Neiteler, R., Brussee, N., Makurat, A., Leu, L, Enzmann, F., Schwarz, J.-O., Wolf, M., Khan, F., Kersten, M., Irvine, S., Stampanoni, M. (2013), Multiphase flow in porous rock imaged under dynamic flow conditions with fast x-ray computed microtomography, SCA2013-011.
6. Dias, M. and Wilkinson, D. (1986), Percolation with trapping, *Journal of Physics A: Mathematical and General*, 19(15), 3131.
7. Georgiadis, A., Berg, S., Makurat, A., Maitland, G., Ott, H. (2013), Pore-scale micro-computed-tomography imaging: Nonwetting-phase cluster-size distribution during drainage and imbibition, *Phys. Rev. E* 88, 033002.

8. Haines, W. B. (1930), Studies in the physical properties of soil. V. The hysteresis effect in capillary properties, and the modes of moisture distribution associated therewith, *The Journal of Agricultural Science*, 20(97), pp. 97-116.

9. Hammond, P, S., Unsal, E., Spontaneous and forced imbibition of aqueous wettability altering surfactant solution into an initially oil-wet capillary, *Langmuir* 25(21), 12591-12603, 2009.

10. Iglauer, S., Paluszny, A., Pentland, C. H., Blunt, M. J. (2011), Residual CO_2 imaged with X-ray micro-tomography, Geophys. Res. Lett. 38, L21403.

11. Joekar-Niasar, V., Hassanizadeh, S. M., Dahle, H. K. (2010), Non-equilibrium effects in capillarity and interfacial area in two-phase flow: dynamic pore-network modeling, J. Fluid Mech. 655, 38-71.

12. Lenormand, R., Zarcone, C., and A. Sarr (1983), Mechanisms of the displacement of one fluid by another in a network of capillary ducts, *Journal of Fluid Mechanics*, 135, pp. 337-353.

13. Masson, Y and Pride, S R. (2014), A Fast Algorithm for Invasion Percolation, *Transport of porous media*, 102 (2), pp. 301-312.

14. Mohanty, K. K., Davis, H. T., and L. E. Scriven (1987), Physics of oil entrapment in water-wet rock, *SPE Reservoir Engineering*, SPE 9406, pp. 113-128.

15. Newman, M. E. (2006), Power laws, Pareto distributions and Zipf's law, arXiv:cond-mat/0412004v3.

16. Patzek, T. W. (2001), Verification of a complete Pore Network Simulator of Drainage and Imbibition *SPE Journal* 6(2), pp. 144–56.

17. Roof, J. G., Snap-off of oil droplets in water-wet pores, SPEJ 10(1), 85-90, 1970.

18. Silin, D, Tomutsa, L., Benson, S., Patzek, T. W. (2010), Microtomography and pore-scale modeling of two-phase fluid distribution. *Transp. Porous Media* 86, 495–515.

19. Vogel, H. J., Tölke, J., Schulz, V. P., Krafczyk, M. Roth, K. (2005), Comparison of a lattice-Boltzmann model, a full morphology model, and a pore network model for determining capillary pressure-saturation relationships. *Vadose Zone J.* 4 , 380–388.

20. Wildenschild, D., Hopmans, J.W., Vaz, C. M. P., Rivers, M. L. (2001), Using x-ray beams to study flow processes in underground porous media. *Adv. Photon Source Res* 4, 48–50.

21. Wilkinson, D and Willemsen, J F. (1983), Invasion Percolation: a new form of percolation theory, *Journal of Physics A: Mathematical and General*, 16(14), 3365.

22. Wilkinson, D. (1986), Percolation effects in immiscible displacement, *Phys. Rev. A* 34 (2), pp. 1380-1391.

23. Huang, D., Honarpour, M. M. (1996), Capillary end effects in coreflood calculations, SCA 9634.